



HAL
open science

Improved relationships between kinetic parameters associated with biomass pyrolysis or combustion

Alain Brillard, Jean-Francois Brillhac

► **To cite this version:**

Alain Brillard, Jean-Francois Brillhac. Improved relationships between kinetic parameters associated with biomass pyrolysis or combustion. *Bioresource Technology*, 2021, 342, pp.126053. 10.1016/j.biortech.2021.126053 . hal-03389206

HAL Id: hal-03389206

<https://hal.science/hal-03389206>

Submitted on 16 Oct 2023

HAL is a multi-disciplinary open access archive for the deposit and dissemination of scientific research documents, whether they are published or not. The documents may come from teaching and research institutions in France or abroad, or from public or private research centers.

L'archive ouverte pluridisciplinaire **HAL**, est destinée au dépôt et à la diffusion de documents scientifiques de niveau recherche, publiés ou non, émanant des établissements d'enseignement et de recherche français ou étrangers, des laboratoires publics ou privés.



Distributed under a Creative Commons Attribution - NonCommercial 4.0 International License

1 **Improved relationships between kinetic parameters** 2 **associated with biomass pyrolysis or combustion**

3

4 Alain BRILLARD^{*,a}, Jean-François BRILHAC^a

5 ^a Université de Haute-Alsace, Laboratoire Gestion des Risques et Management UR2334, 3bis
6 rue Alfred Werner, 68093 Mulhouse Cedex, France

7

8 **Abstract**

9 Improved relationships between the kinetic parameters (pre-exponential factor and kinetic
10 energy) associated with biomass pyrolysis or combustion processes are proposed. These
11 relationships rely on observations of the mass and mass rate curves and on the experimental
12 data through computations performed on the kinetic model which describes the mass
13 evolution of each pseudo-component of the biomass during its thermal degradation. These
14 relationships improve the so-called kinetic compensation effect. They are here implemented
15 as part of the Extended Independent Parallel Reaction (EIPR) model.

16

17 **Keywords:** Kinetic modeling; Optimal kinetic parameters; Kinetic compensation effect;
18 Biomass thermal degradation; EIPR model

19

* Corresponding author. Alain.Brillard@uha.fr

20 **1. Introduction**

21 Many papers have already been published which deal with the kinetic modeling of biomass
22 pyrolysis or combustion under low temperature ramps. Different methods or models are
23 available to simulate the thermal degradation of a material.

24 Differential or integral isoconversional methods are presented in (Vyazovkin et al., 2011).
25 They start from the single first-order differential equation which describes the evolution of
26 the sample extent of conversion with respect to time. Such methods do not solve this
27 differential equation. The Extended Independent Parallel Reaction (EIPR) model assumes the
28 presence of pseudo-components or constituents of the biomass submitted to thermal
29 degradation, for example hemicellulose, cellulose, lignin and char. These constituents are
30 supposed to decompose in an almost independent way, (Amutio et al., 2012; Babu, 2008;
31 Collard and Blin, 2014; Dhyani and Bhaskar, 2018). Comparisons between the differential
32 and integral isoconversional methods and the EIPR method are indicated in Table 1.

33 **Table 1.**

34 Using the isoconversional methods is quite simple, as they do not require a software
35 dedicated to the resolution of the underlying ordinary differential equation. Nevertheless,
36 these isoconversional methods often fail to simulate the mass and mass rate curves in a
37 satisfying way, especially when multiple processes occur during the thermal degradation of
38 the material, see for example (Brillard et al., 2017) in the case the thermal degradation of
39 cellulose and cotton samples.

40 The independence assumption of the EIPR model is certainly a rough simplification of the
41 complex processes which occur during the pyrolysis or combustion of a biomass.

42 Nevertheless, this assumption is evoked in (Vyazovkin et al., 2011) and is used in (Dhahak et

43 al., 2019) who applied Ranzi's scheme presented for example in (Debiagi et al., 2015) to
44 simulate the combustion of beech, fir and oak woods. The overall resolution process through
45 the EIPR model requires a dedicated software and simultaneously returns the simulated
46 mass and mass rate curves. Error measurements between the experimental and simulated
47 mass and mass rate curves returned from the resolution are used to validate the optimal
48 values of the kinetic parameters.

49 The Distributed Activation Energy Model (DAEM) may be used to simulate the thermal
50 degradation of a biomass. It considers a single first-order differential equation for each
51 constituent of a biomass, but with a continuous distribution of activation energies having a
52 density $f(E)$ which is usually taken as a Gaussian, Weibull or logistic function. The DAEM
53 model is based on the conversion of the first-order differential equation of the kinetic model
54 to an integral whose computation requires a software and numerical tools.

55 Solving the single ordinary differential equation or system of ordinary differential equations
56 and determining the optimal sets of kinetic parameters through the EIPR or DAEM models
57 takes a quite long time if the number of experimental times and data is high (usually many
58 thousands). To reduce the number of experimental time points without decreasing the
59 quality of the simulation, a selection of them is usually done. Nevertheless, the number of
60 stages to be taken into account in the thermal degradation cannot be reduced and the
61 computational time also highly increases with this number of stages. Trying to establish
62 relationships between the kinetic parameters or laws predicting some kinetic parameters
63 was the topic of different papers. Criado et al. suggested a power law function of the
64 temperature for the pre-exponential factor, (Criado et al., 2005). The kinetic compensation
65 effect expresses a relationship between the logarithm of the pre-exponential factor A and

66 the activation energy Ea through an affine relation whose model-free coefficients only
67 depend on the temperature rate, (Galwey, 2004; Vyazovkin et al., 2011).

68 The present study proposes improved relationships between the pre-exponential factor and
69 the activation energy associated with each constituent of a biomass submitted to pyrolysis
70 or combustion. These relationships are deduced from observations of the experimental mass
71 and mass rate curves and from the experimental data, through quite easy computations
72 performed on the first-order differential equation or system of equations associated with
73 the kinetic model. These relationships divide by two the number of kinetic parameters to be
74 determined in the kinetic model. For example, only the activation energy associated with
75 each constituent has to be determined, the pre-exponential factor being deduced from the
76 corresponding relationship. These relationships generalize the so-called kinetic
77 compensation effect. In the present study, these relationships are implemented in four
78 examples concerning the pyrolysis or combustion of different biomass. The simulations are
79 performed using the EIPR model. In each case, different error measurements and the
80 computational times are computed and compared when considering either the classical
81 resolution or that involving the relationships. The error measurements prove that the
82 resolution through the EIPR model which involves the relationships leads to slightly better
83 simulations of the mass and mass rate curves than that using the classical resolution and in a
84 lower computational time. The reduction of the computational time is further observed to
85 become highly significant when the number of constituents to be considered in the thermal
86 degradation process increases. Even if these relationships are here implemented within the
87 framework of the EIPR model, they can surely be used in other models, for example the
88 DAEM one.

89

90 **2. Materials and methods**

91 **2.1. Materials and thermogravimetric experiments**

92 The present study relies on pyrolysis experiments previously performed on pure cellulose
93 and palm nut shell, or on combustion experiments also previously performed on cotton
94 residue and coffee husk. Cellulose is the main constituent of the biomass. It is a linear chain
95 of D-glucose molecules. Cotton contains approximately 98% of cellulose. The pyrolysis and
96 combustion processes of pure cellulose and of cotton samples were analyzed and simulated
97 in (Brillard et al., 2017). Palm nut shells are by-products of palm oil production. They are
98 obtained after extraction of palm oil, grinding of the nut, and extraction of almonds from the
99 nuts. Palm nut shells were provided by a Cameroonian Joint Initiative Group. The coffee husk
100 is the envelope of coffee beans. Coffee husks were collected from a Cameroonian coffee
101 peeling factory. The pyrolysis and combustion processes of palm nut shells and of coffee
102 husks were analyzed and simulated in (Vitoussia et al., 2019).

103 Different characterizations were performed on these materials: proximate and ultimate
104 analyses and calorific values. Their results can be found in the above-indicated papers.

105 Thermogravimetric experiments were performed on these materials in a thermobalance TA
106 Q500 Texas Instruments from room temperature to 900 °C, under pure nitrogen or under
107 synthetic air and under different low temperature rates (5, 10, 15, and 20 °C/min). More
108 details concerning the thermogravimetric experiments can be found in the above-indicated
109 papers. In the present study, only the thermal degradations under a temperature ramp of 5
110 °C/min are considered. However, thermal degradations under other temperature ramps can
111 be efficiently simulated with the tools of the present study.

112

113 **2.2. Relationships between kinetic parameters**

114 The improved relationships between kinetic parameters which are proposed in the present
115 study are established in four cases, starting from the simplest case and ending with the more
116 complex one:

- 117 • A pyrolysis process occurring in a single stage (pure cellulose).
- 118 • A pyrolysis process occurring in multiple stages (palm nut shell sample, whose mass
119 rate curve presents two peaks and a long tail).
- 120 • A combustion process (cotton sample) occurring in a single devolatilization stage,
121 which is simulated with the Avrami-Erofeev reaction function of order 4, followed by
122 the char combustion stage simulated with the first-order reaction function (Mampel).
- 123 • A combustion process occurring in multiple stages (coffee husk sample).

124 During a pyrolysis process applied to a biomass, volatiles (CO, CO₂ and organic compounds)
125 are being emitted mainly between 150 and 600 °C. At the end of the pyrolysis process, the
126 char structure and the ash are remaining. Considering the lignocellulosic representation of
127 biomass, cellulose is usually the main component of a biomass. Cellulose pyrolysis occurs in
128 two or three stages, the first one being the constitution of active cellulose. Then saccharides,
129 cellulose, furanes and other molecules appear, according to the so-called Broido's models,
130 (Bradbury et al., 1979), (Richter and Rein, 2017). Hemicellulose is built in small chains of
131 sugar units (xylose, arabinose, mannose, galactose, rhamnose). Its pyrolysis occurs in two
132 steps, (Huang et al., 2017), the authors here focusing on the primary step. Lignin fills the
133 spaces in the cell wall between cellulose and hemicellulose. It is composed of cross-linked
134 phenolic precursors. Its pyrolysis occurs in two stages, (Raveendran, 1996). The reaction

135 processes of biomass pyrolysis are analyzed in (Wang et al., 2017), (Várhegyi et al., 1997).
136 Biomass pyrolysis is one route to the production of valuable by-products.
137 The combustion of cellulose was analyzed in (Shafizadeh and Bradbury, 1979) and compared
138 to its pyrolysis. Reaction mechanisms were here proposed. The biomass combustion may be
139 decomposed in different stages: moisture evaporation, pyrolysis with gas production, char
140 combustion, and gas oxidation. The volatiles are usually emitted at slightly lower
141 temperatures and with higher rates during a combustion process than during a pyrolysis
142 process. Then the char structure is being degraded. Ash are the only remaining elements at
143 the end of the combustion process. In (Jenkins et al., 1998), the authors present a single,
144 long, and incomplete equation which accounts for the biomass combustion and they give the
145 values of the fifteen involved coefficients for hybrid poplar and rice straw. The biomass
146 combustion essentially leads to energy and heat production.

147 **2.2.1. Relationship between the kinetic parameters when simulating a pyrolysis**
148 **process occurring in a single stage with a general reaction function**

149 When submitting a pure cellulose sample to pyrolysis, a unique devolatilization peak is
150 observed, see (Brillard et al., 2017) and also the solid line curve of Fig. 1 b), section 3.1.1. In
151 some cases corresponding to intense pyrolysis processes like that of pure cellulose, an
152 Avrami-Erofeev reaction function may be chosen among the many available ones described
153 in (Vyazovkin et al., 2011) for example, to well simulate the pyrolysis process. In such case,
154 the kinetic model is usually written in terms of the extent of conversion given at time t as:

155
$$\alpha(t) = \frac{m_{ini} - m_s(t)}{m_{ini} - m_{fin}} \leftrightarrow m_s(t) = m_{ini} - \alpha(t)(m_{ini} - m_{fin}), \quad (1)$$

156 as the first-order differential equation:

157
$$\alpha'(t) = k(T(t))f(\alpha(t)). \quad (2)$$

158 Differentiating this equation (2) with respect to time leads to:

159
$$\alpha''(t) = \frac{EaT'(t)}{RT^2(t)} k(T(t))f(\alpha(t)) + (k(T(t)))^2 f'(\alpha(t))f(\alpha(t))$$

160
$$= k(T(t))f(\alpha(t)) \left(\frac{EaT'(t)}{RT^2(t)} + k(T(t))f'(\alpha(t)) \right). \quad (3)$$

161 From the definition (1) of the extent of conversion, the derivative of the mass sample is
 162 expressed as: $m'_s(t) = -\alpha'(t)(m_{ini} - m_{fin})$, whence the second derivative of the sample
 163 mass is expressed as: $m''_s(t) = -\alpha''(t)(m_{ini} - m_{fin})$. The opposite of the sample mass rate
 164 reaches a maximum at t^* , which implies that the second-order derivative of the extent of
 165 conversion is equal to 0 at t^* . This leads to the relationship between the two kinetic
 166 parameters A and Ea expressed as:

167
$$\frac{EaT'(t^*)}{RT^2(t^*)} + k(T(t^*))f'(\alpha(t^*)) = 0 \leftrightarrow A = -\frac{EaT'(t^*)}{RT^2(t^*)} \exp\left(\frac{Ea}{RT(t^*)}\right) \frac{1}{f'(\alpha(t^*))}. \quad (4)$$

168 This relationship (4) involves the temperature $T(t^*)$ at t^* , the temperature rate $T'(t^*)$ and
 169 also the extent of conversion $\alpha(t^*)$ at t^* . The time t^* at which the opposite of the mass rate
 170 takes its maximum has to be found in the experimental data, together with the temperature
 171 $T(t^*)$. The extent of conversion $\alpha(t^*)$ at this time t^* has also to be found or computed
 172 through its definition (1) from the experimental data.

173 In the case where the reaction function is the first-order one (Mampel), the computations
 174 leading to the improved relationship between the kinetic parameters can be performed on
 175 the kinetic model which considers the evolution of the mass of volatiles m_{vol} instead of the
 176 extent of conversion (not shown here).

177 The relationship (4) is slightly more complex than the kinetic compensation effect indicated
178 in (Vyazovkin et al., 2011) and expressed as: $\ln(A) = aEa + b$, for model-free parameters a
179 and b which depend on the heating rate. This relationship was used by many authors (Czajka
180 et al., 2016; Ojha et al., 2017), for example, and also when applying the DAEM model (Huang
181 et al., 2017; Xu et al., 2018), for example.

182 **2.2.2. Relationship between the kinetic parameters when simulating a pyrolysis** 183 **process occurring in multiple stages**

184 The pyrolysis of palm nut shell presents multiple stages, see (Vitoussia et al., 2019) and also
185 the solid line curves of Fig. 2, section 3.1.2. In this case, the mass rate curve of Fig. 2 b)
186 presents a first small peak before 150 °C which corresponds to the moisture evaporation
187 stage. This stage will not be considered in the simulations. Then two thin peaks appear
188 between 250 and 350 °C. Between these two peaks, the mass rate does not go down to 0
189 %/s. On the right-hand side of the second peak, a long tail appears until 750-800 °C.

190 On the mass curve of Fig. 2 a), a first small decrease appears before 150 °C. Then a high
191 decrease occurs between 250 and 350°C with a change of slope. Above 350 °C, the mass
192 goes on decreasing until 750-800 °C.

193 These changes of slope or peaks and tail may be explained by the presence of different
194 constituents which are being devolatilized in different but possibly superimposing
195 temperature ranges. Omitting the moisture evaporation stage, four constituents will be
196 considered in the EIPR model which will be applied to simulate this pyrolysis process.

197 Besides the hemicellulose and cellulose constituents of a lignocellulosic material, lignin
198 usually decomposes in two stages, (Jiang et al., 2018; Kawamoto, 2017).

199 In this pyrolysis case, the EIPR model consists in a set of ordinary differential equations. Each
 200 first-order ordinary differential equation is written as:

$$201 \quad \frac{dm_{vol,i}^e}{dt}(t) = k_i(T(t))f(m_i(0) - m_{vol,i}^e(t)), i = 1, \dots, I, \quad (5)$$

202 where $m_{vol,i}^e(t)$ (kg) is the mass of volatiles emitted from the constituent i of the sample
 203 ($i=1, \dots, I$) and $m_i(0)$ (kg) is the initial mass of the constituent i . The kinetic constant $k_i(T)$
 204 obeys an Arrhenius law: $k_i(T) = A_i \exp(-Ea_i/RT)$, where A_i (1/s) (resp. Ea_i (J/mol)) is the
 205 pre-exponential factor (resp. the activation energy) associated with the constituent i .

206 The initial value $m_{vol,i}^e(0)$ of volatiles emitted from the constituent i is equal to 0 kg.

207 For each constituent, the relationship (4) can be used which give the value of the pre-
 208 exponential factor A_i in terms of the activation energy Ea_i and of the time t_i^* at which the
 209 mass of volatiles emitted from the constituent i is maximal, according to:

$$210 \quad A_i = -\frac{Ea_i T'(t_i^*)}{RT^2(t_i^*)} \exp\left(\frac{Ea_i}{RT(t_i^*)}\right) \frac{1}{f'(\alpha(t_i^*))}. \quad (6)$$

211 In each relationship (6), the time t_i^* at which the mass rate of volatiles emitted from the
 212 constituent i is maximal has to be determined first observing the experimental mass rate
 213 curve and analyzing the experimental data. This is easy in the case of a well identified peak.
 214 In the cases of a tail or of a shoulder, the determination of this time t_i^* is more complicated.

215 **2.2.3. Relationship between the kinetic parameters when simulating a combustion** 216 **process with a single devolatilization stage**

217 The combustion of a cotton sample was analyzed in (Brillard et al., 2017). A unique
 218 devolatilization peak may be observed, which is followed by a unique char combustion peak,

219 see also the solid line curve of Fig. 3 b), section 3.2.1. Cotton is composed of cellulose up to
 220 98%. This unique constituent contains a fraction τ_{vol} of volatiles to be emitted and the
 221 remaining fraction $1 - \tau_{vol}$ of char to be consumed in the final stage of the combustion
 222 process. Here the devolatilization stage occurs between 200 and 350 °C. The char
 223 combustion stage occurs between 350 and 470 °C. Above 470 °C, the mass rate is almost
 224 equal to 0 g/s and the mass is stable at 2.2×10^{-3} g, the remaining ash weight.

225 In this case, the kinetic system is written in terms of the extent of conversion α_{vol} defined
 226 through $\alpha_{vol}(t) = m_{vol}(t) / (\tau_{vol}(m_{ini} - m_{fin}))$ as:

$$227 \quad \begin{cases} \alpha'_{vol}(t) = k_{vol}(T(t))f(\alpha_{vol}(t))\frac{1}{\tau_{vol}} \\ m'_{char}(t) = k_{comb}(T(t))\left(\frac{1 - \tau_{vol}}{\tau_{vol}}m_{vol}(t) - m_{char}(t)\right)P_{O_2}, \end{cases} \quad (7)$$

228 Differentiating the first equation of (7) with respect to time leads to:

$$229 \quad \alpha''_{vol}(t) = k_{vol}(T(t))\frac{Ea_{vol}T'(t)}{RT(t)^2}f(\alpha_{vol}(t))\frac{1}{\tau_{vol}} \\ 230 \quad + k_{vol}(T(t))f'(\alpha_{vol}(t))k_{vol}(T(t))f(\alpha_{vol}(t))\frac{1}{(\tau_{vol})^2}. \quad (8)$$

231 At the time t^* where the devolatilization peak reaches its maximum, this second derivative
 232 cancels. This leads to the relationship:

$$233 \quad A_{vol} = -\frac{\tau_{vol}}{f'(\alpha_{vol}(t^*))}\frac{Ea_{vol}T'(t^*)}{RT^2(t^*)}\exp\left(\frac{Ea_{vol}}{RT(t^*)}\right), \quad (9)$$

234 which has the same structure as (4).

235 Differentiating the second equation of (7) with respect to time leads to:

$$\begin{aligned}
236 \quad m''_{char}(t) &= k_{comb}(T(t)) \frac{Ea_{comb}T'(t)}{RT(t)^2} \left(\frac{1-\tau_{vol}}{\tau_{vol}} m_{vol}(t) - m_{char}(t) \right) P_{O_2} \\
237 \quad &+ k_{comb}(T(t)) \left(\frac{1-\tau_{vol}}{\tau_{vol}} m'_{vol}(t) - m'_{char}(t) \right) P_{O_2} \\
238 \quad &= k_{comb}(T(t)) \frac{Ea_{comb}T'(t)}{RT(t)^2} \left(\frac{1-\tau_{vol}}{\tau_{vol}} m_{vol}(t) - m_{char}(t) \right) P_{O_2} \\
239 \quad &+ k_{comb}(T(t)) \left(\frac{1-\tau_{vol}}{\tau_{vol}} (m_{ini} - m_{fin}) k_{vol}(T(t)) f(\alpha_{vol}(t)) \right. \\
240 \quad &\left. - k_{comb}(T(t)) \left(\frac{1-\tau_{vol}}{\tau_{vol}} m_{vol}(t) - m_{char}(t) \right) P_{O_2} \right) P_{O_2}. \quad (10)
\end{aligned}$$

241 At the time t^{**} where the second derivative $m''_{char}(t)$ is equal to 0, (10) becomes

$$\begin{aligned}
242 \quad 0 &= \left(\frac{Ea_{comb}T'(t^{**})}{RT(t^{**})^2} - k_{comb}(T(t^{**}))P_{O_2} \right) \left(\frac{1-\tau_{vol}}{\tau_{vol}} m_{vol}(t^{**}) - m_{char}(t^{**}) \right) \\
243 \quad &+ \frac{1-\tau_{vol}}{\tau_{vol}} (m_{ini} - m_{fin}) k_{vol}(T(t^{**})) f(\alpha_{vol}(t^{**})). \quad (11)
\end{aligned}$$

244 Defining the terms:

$$245 \quad \alpha = \frac{1-\tau_{vol}}{\tau_{vol}} m_{vol}(t^{**}) - m_{char}(t^{**}), \quad (12)$$

$$246 \quad \beta = \frac{1-\tau_{vol}}{\tau_{vol}} (m_{ini} - m_{fin}) k_{vol}(T(t^{**})) f(\alpha_{vol}(t^{**})), \quad (13)$$

247 the equation (11) leads to the following relationship between A_{comb} and Ea_{comb} :

$$248 \quad A_{comb} = \frac{1}{P_{O_2}} \exp\left(\frac{Ea_{comb}}{RT(t^{**})}\right) \left(\frac{Ea_{comb}T'(t^{**})}{RT(t^{**})^2} + \frac{\beta}{\alpha} \right). \quad (14)$$

249 In the case where the reaction function associated with the devolatilization stage is the first-
250 order one (Mampel), the computations leading to the improved relationship between the

251 kinetic parameters can again be performed on the kinetic model whose first equation
252 considers the evolution of the mass of volatiles m_{vol} instead of the extent of conversion (not
253 shown here).

254 **2.2.4. Relationship between the kinetic parameters in the case of a combustion** 255 **process whose devolatilization occurs in multiple stages**

256 The combustion of a coffee husk sample occurs in multiple stages, (Vitoussia et al., 2019),
257 see also the solid line curves of Fig. 4, section 3.2.2. The mass rate curve (solid line curve of
258 Fig. 4 b)) presents a first peak which ends before 150 °C and which corresponds to the
259 moisture evaporation. A second peak which occurs between 150 and 350 °C and with
260 shoulders on its both sides and which corresponds to the devolatilization of the sample.
261 Finally, a third peak which occurs between 350 and 480 °C and which corresponds to the
262 char combustion.

263 As in the preceding simulations, the moisture evaporation stage will not be considered in the
264 present study, although the mass loss is here relatively important. Five stages may be
265 considered respectively corresponding to the two peaks, the shoulders on both sides of the
266 first peak and the important degradation of a constituent of the material around 370 °C.
267 Notice that in the present situation, the char combustion peak has almost the same size as
268 the devolatilization peak.

269 In this combustion case, the relationships between the kinetic parameters associated with
270 the devolatilization stages through (9) are used to divide by two the number of unknown
271 parameters. The relationship (14) is used for the simulation of the char combustion.

272

273 2.2.5. Simulations through the EIPR model and error measurements

274 In the present study, the Extended Independent Parallel Reaction model is used to simulate
275 the thermal degradations of the different samples under consideration. The first reason is
276 that this model preserves the differential equation or system which describes the evolution
277 of the devolatilization or of the char combustion with respect to time. The second reason is
278 that solving the EIPR model directly returns simulations of the mass and mass rate curves,
279 together with error measurements and computational time.

280 The EIPR model consists to solve the kinetic equation or system (2), (5), or (7), depending on
281 the thermal degradation process, first with initial guesses of the kinetic parameters. In the
282 present simulations, these initial guesses of the kinetic parameters are chosen not too far
283 and not too close from the final values. The routine 'ode' of the Scilab software (version
284 6.0.2) is here used. The optimal values of the kinetic parameters are obtained minimizing the
285 objective function chosen as:

$$286 \sum_{j=1}^N \left(\left(\frac{dm_{vol,i}^e}{dt} \right)_{exp} (t_j) - \left(\frac{dm_{vol,i}^e}{dt} \right)_{sim} (t_j) \right)^2, \quad (15)$$

287 through the routine 'datafit' of Scilab. This objective function indeed led to a unique
288 minimizer in a neighborhood of the optimal set of kinetic parameters, (Brillard and Brillhac,
289 2020). In (15), N is the overall number of experimental time points. The equations or
290 systems (2), (5), or (7) are finally solved with the optimal values again using the routine
291 'ode' and the code returns the simulated mass and mass rate curves.

292 To validate these simulations, different error measurements are considered:

- 293 - the maximal difference between the experimental and simulated mass rate curves,
294 hereafter denoted as l_{∞} (kg/s),

- 295 - the square root of the squared difference between the experimental and simulated
296 mass rate curves, hereafter denoted as l_2 (kg/s),
297 - R^2 determination coefficients for the mass R_m^2 , mass rate R_{mr}^2 and overall R_o^2
298 variations. These determination coefficients should be as close to 1 as possible to
299 validate the simulations.

300 The precise expressions of these error measurements can be found for example in (Brillard
301 et al., 2021).

302 The computations associated with the five cases evoked in subsection 2.2 are performed
303 using the classical (without the relationships between pre-exponential factor and activation
304 energy) and improved (taking into account the relationships between the kinetic
305 parameters) EIPR models on a DELL Latitude 5400 laptop through the free Scilab software
306 version 6.0.2 and some of its routines. Every software able to read experimental data as
307 returned by the thermobalance, to solve a differential equation and to minimize an objective
308 function associating the experimental and simulated data with respect to the kinetic
309 parameters to be determined can be used with success.

310

311 **3. Results and discussion**

312 **3.1. Simulations of pyrolysis processes**

313 **3.1.1. Simulation of a pyrolysis process occurring in a single stage a second-order**

314 **Avrami-Erofeev reaction function (cellulose sample)**

315 The sample containing a single component (cellulose), the mass rate curve presents a simple
316 shape with a unique devolatilization peak, see Fig. 1 b) below. Because this unique
317 devolatilization peak occurs between 200 and 300 °C, the simulations are performed in the

318 temperature range 150-450 °C. An Avrami-Erofeev function of order 2 defined in terms of
319 the extent of conversion α through:

$$320 \quad f_2(\alpha) = 2(1 - \alpha)(-\log(1 - \alpha))^{0.25}, \quad (16)$$

321 is used. 5221 experimental times are considered. According to Fig. 1 b) and to the
322 experimental data, the temperature at which the maximal mass rate is reached is equal to
323 336.19 °C and the corresponding time t^* is equal to 106.8 s.

324 Nevertheless, choosing the temperature $T(t^*)$ at which the maximal mass rate is reached
325 equal to 336.19 °C and the corresponding time t^* equal to 106.8 s leads to not totally
326 satisfying simulations (not shown here) when applying the improved EIPR model. Choosing
327 instead the temperature $T(t^*)$ at which the maximal mass rate is reached equal to 339.75 °C
328 (+3.56 °C) and the corresponding time t^* equal to 107.6 s (+0.8 s) leads to better simulation
329 results, see Fig. 1. Table 2 gathers the initial and optimal values of the kinetic parameters
330 determined through the classical and improved EIPR models, the different error
331 measurements and the computational times.

332 **Table 2.**

333 The optimal values of the kinetic parameters differ, being slightly greater for the improved
334 model than for the classical one. The error measurements are slightly better for the
335 improved model than for the classical one. The computational time for this improved EIPR
336 model is lower than that of the classical one.

337 The simulations with the classical and improved EIPR models are gathered in Fig. 1.

338 **Figure 1.**

339 It is difficult to identify the simulated mass and mass rate curves as they quite perfectly
340 superimpose. The simulated mass curves are below the experimental one and the simulated
341 mass rate curve start a little bit earlier and they go back to 0 a little bit earlier than the
342 experimental one. The maximal mass rate of the improved EIPR model is reached at 339.29
343 °C, while that of the classical EIPR model is reached at 338.85 °C.

344 **3.1.2. Simulations of a pyrolysis process with multiple stages (palm nut shell sample)**

345 The pyrolysis process of a palm nut shell under nitrogen and a temperature ramp of 5 °C/min
346 occurs in four stages, see the solid line curves of Fig. 2 below. This presence of four stages is
347 the consequence of three components (hemicellulose, cellulose and lignin) in the biomass
348 which decompose in different but possibly superimposing temperature ranges. The fractions
349 of these three components were determined in (Vitoussia et al., 2019) applying Van Soest's
350 protocol. The chosen fractions of the initial mass of the four constituents are taken equal to:
351 0.27, 0.30, 0.24 and 0.19, as estimated from the relative importance of the peaks or tail of
352 Fig. 2 b).

353 For the improved model, the temperatures $T(t^*)$ which correspond to the maximal
354 devolatilization of each constituent are determined equal to: 270.5, 342.1, 319.0, and 362.2
355 °C, respectively, corresponding to the times 5708, 6567, 6290, and 6809 s. 12588
356 experimental times and data are used corresponding to temperatures between 150 and 850
357 °C.

358 The initial guesses and the optimal values of the kinetic parameters are gathered in Table 3,
359 together with the error measurements and the computational times.

360 **Table 3.**

361 The optimal values of the activation energies are almost the same for both models and they
362 do not differ so much from the initial values. The optimal values of the pre-exponential
363 factors slightly differ. The error measurements are slightly better with the improved EIPR
364 model when compared to that of the classical one. The computational time with the classical
365 model is approximately equal to five times that with the improved model. Taking into
366 account the relationships (6) in the simulations with the EIPR model significantly reduces the
367 computational time and increases the quality of these simulations.

368 The experimental and simulated mass and mass rate curves are gathered in Fig. 2.

369 **Figure 2.**

370 The simulated mass curve are both slightly below the experimental one. The simulated mass
371 rate curves start a little bit too early. Nevertheless, the determination coefficients are
372 sufficiently high to accept the simulations, with slightly higher values for the improved
373 model.

374 **3.2. Simulation of combustion processes**

375 **3.2.1. Simulation of a combustion process with a single devolatilization stage**

376 As already indicated, cotton is composed of cellulose up to 98%. A unique and very thin
377 devolatilization peak appears in the mass rate curve which is followed by a small char
378 combustion peak, see the solid line curve of Fig. 3 b).

379 To simulate in an appropriate way the thinness of the devolatilization peak, an Avrami-
380 Erofeev or order 4 is used which is given as:

$$381 \quad f_4(\alpha) = 4(1 - \alpha)(-\log(1 - \alpha))^{0.75}. \quad (17)$$

382 1033 experimental times are used between room temperature and 900 °C. The proportion
383 τ_{vol} of volatiles is taken equal to 0.86, whence that of char τ_{char} is equal to 0.14. The time t^*
384 at which the maximal devolatilization rate is reached is taken equal to 4150 s, corresponding
385 to a temperature equal to 323.01 °C. This temperature $T(t^*)$ is slightly smaller than the
386 temperature (339.75 °C) at which the devolatilization peak reached its maximum during the
387 pyrolysis process of the pure cellulose sample. The maximal height of this devolatilization
388 peak is equal to 0.24 in the pyrolysis case and to 0.33 in the combustion case. Oxygen is
389 known to enhance the degradation process. The time t^{**} at which the maximal char
390 combustion rate was reached is taken equal to 5550 s, corresponding to a temperature
391 equal to 439.59 °C.

392 According to the procedure described in subsection 2.2.3, the initial and optimal values of
393 the kinetic parameters are gathered in Table 4, together with the error measurements and
394 the computational times for the classical and improved EIPR models.

395 **Table 4.**

396 With the improved EIPR model, the kinetic parameters are significantly changed. The error
397 measurements are very slightly worse, but the computational time is divided by more than
398 2.

399 The experimental and simulated mass and mass rate curves are gathered in Fig. 3.

400 **Figure 3.**

401 It is difficult to identify the two simulated mass curves as they do well superimpose. For the
402 mass rate curves, that with the improved EIPR model presents a char combustion peak
403 slightly higher than the experimental one. This is coherent with the values of the kinetic

404 parameters presented in Table 4. Part of these very slightly worse error measurements and
405 slightly too high simulated char combustion peak may be explained by the absence of a
406 further constituent in the cotton sample (apart from cellulose). The mass rate curve does not
407 go down to 0 between the devolatilization and char combustion peaks, possibly due to the
408 presence of a further constituent in the cotton sample.

409 **3.2.2. Simulation of a combustion process whose devolatilization occurs in multiple** 410 **stages**

411 Five constituents, plus the char, were considered for the devolatilization of the coffee husk
412 sample. Their respective fractions are chosen equal to: 0.08, 0.40, 0.06, 0.26, and 0.20. The
413 proportions of volatiles in each constituent were respectively chosen equal to: 0.60, 0.58,
414 0.65, 0.55, and 0.53. Mampel's reaction function is here used for the devolatilization of the
415 five constituents. 11998 experimental times and data are considered.

416 The initial and optimal values of the kinetic parameters returned by the classical and
417 improved EIPR models are gathered in Table 5.

418 **Table 5.**

419 With the improved EIPR model, the pre-exponential factors are significantly changed, the
420 error measurements are slightly better than that of the classical model and the
421 computational time is divided by more than 7. The kinetic model involves six pairs of kinetic
422 parameters and the EIPR model involving the relationships between the kinetic parameters
423 is especially efficient in this case.

424 The experimental and simulated mass and mass rate curves are gathered in Fig. 4.

425 **Figure 4.**

426 The simulated mass and mass rate curves returned by both models are quite well
427 superimposed. However, the error measurements are slightly better when applying the
428 improved EIPR model and the computational time is much smaller.

429

430 **4. Conclusion**

431 Improved relationships were established between the pre-exponential factor and the
432 activation energy associated with each constituent of a biomass submitted to pyrolysis or
433 combustion under low temperature ramps. They only involve experimental data through
434 easy computations on the equations of the underlying model. Simulations performed using
435 the EIPR model for different biomass proved that the error measurements between the
436 experimental and simulated mass and mass rate curves are slightly improved using these
437 relationships. The computational time is here significantly reduced, especially in the cases
438 where multiple constituents are taken into account in the kinetic model.

439

440 **Acknowledgments**

441 The authors thank Mrs Chloée Roumegoux and Dr. Théophile Vitoussia for the
442 thermogravimetric experiments they performed under the supervision of Mrs. Damaris
443 Kehrli respectively on cellulose and cotton samples, and on coffee husks and palm nut shells.

444

445 **This research did not receive any specific grant from funding agencies in the public,**
446 **commercial, or not-for-profit sectors.**

447

- 449 1. Amutio, M., Lopez, G., Aguado, R., Artetxe, M., Bilbao, J., Olazar, M., 2012. Kinetic study of
450 lignocellulosic biomass oxidative pyrolysis. *Fuel* 95, 305–311.
451 <https://doi.org/10.1016/j.fuel.2011.10.008>
- 452 2. Babu, B.V., 2008. Biomass pyrolysis: a state-of-the-art review. *Biofuels, Bioprod. Bioref.* 2,
453 393–414. <https://doi.org/10.1002/bbb.92>
- 454 3. Bradbury, A.G.W., Sakai, Y., Shafizadeh, F., 1979. A kinetic model for pyrolysis of cellulose.
455 *J. Appl. Polym. Sci.* 23, 3271–3280. <https://doi.org/10.1002/app.1979.070231112>
- 456 4. Brillard, A., Brilhac, J.F., 2020. Improvements of global models for the determination of
457 the kinetic parameters associated to the thermal degradation of lignocellulosic
458 materials under low heating rates. *Renewable Energy* 146, 1498–1509.
459 <https://doi.org/10.1016/j.renene.2019.07.040>
- 460 5. Brillard, A., Habermacher, D., Brilhac, J.-F., 2017. Thermal degradations of used cotton
461 fabrics and of cellulose: kinetic and heat transfer modeling. *Cellulose* 24, 1579–1595.
462 <https://doi.org/10.1007/s10570-017-1200-6>
- 463 6. Brillard, A., Kehrl, D., Douguet, O., Gautier, K., Tschamber, V., Bueno, M.-A., Brilhac, J.-F.,
464 2021. Pyrolysis and combustion of community masks: Thermogravimetric analyses,
465 characterizations, gaseous emissions, and kinetic modeling. *Fuel* 306, 121644.
466 <https://doi.org/10.1016/j.fuel.2021.121644>
- 467 7. Collard, F.-X., Blin, J., 2014. A review on pyrolysis of biomass constituents: Mechanisms
468 and composition of the products obtained from the conversion of cellulose,
469 hemicelluloses and lignin. *Renewable and Sustainable Energy Reviews* 38, 594–608.
470 <https://doi.org/10.1016/j.rser.2014.06.013>
- 471 8. Criado, J.M., Pérez-Maqueda, L.A., Sánchez-Jiménez, P.E., 2005. Dependence of the
472 preexponential factor on temperature: Errors in the activation energies calculated by
473 assuming that A is constant. *J Therm Anal Calorim* 82, 671–675.
474 <https://doi.org/10.1007/s10973-005-0948-3>
- 475 9. Czajka, K., Kisiela, A., Moroń, W., Ferens, W., Rybak, W., 2016. Pyrolysis of solid fuels:
476 Thermochemical behaviour, kinetics and compensation effect. *Fuel Processing*
477 *Technology* 142, 42–53. <https://doi.org/10.1016/j.fuproc.2015.09.027>
- 478 10. Debiagi, P.E.A., Pecchi, C., Gentile, G., Frassoldati, A., Cuoci, A., Faravelli, T., Ranzi, E.,
479 2015. Extractives Extend the Applicability of Multistep Kinetic Scheme of Biomass
480 Pyrolysis. *Energy Fuels* 29, 6544–6555.
481 <https://doi.org/10.1021/acs.energyfuels.5b01753>
- 482 11. Dhahak, A., Hild, G., Rouaud, M., Mauviel, G., Burkle-Vitzthum, V., 2019. Slow pyrolysis of
483 polyethylene terephthalate: Online monitoring of gas production and quantitative
484 analysis of waxy products. *Journal of Analytical and Applied Pyrolysis* 142, 104664.
485 <https://doi.org/10.1016/j.jaap.2019.104664>
- 486 12. Dhyani, V., Bhaskar, T., 2018. A comprehensive review on the pyrolysis of lignocellulosic
487 biomass. *Renewable Energy* 129, 695–716.
488 <https://doi.org/10.1016/j.renene.2017.04.035>
- 489 13. Galwey, A.K., 2004. Is the science of thermal analysis kinetics based on solid
490 foundations? *Thermochimica Acta* 413, 139–183.
491 <https://doi.org/10.1016/j.tca.2003.10.013>
- 492 14. Huang, Y.W., Chen, M.Q., Li, Y., 2017. An innovative evaluation method for kinetic
493 parameters in distributed activation energy model and its application in

- 494 thermochemical process of solid fuels. *Thermochimica Acta* 655, 42–51.
495 <https://doi.org/10.1016/j.tca.2017.06.009>
- 496 15. Jenkins, B.M., Baxter, L.L., Miles, T.R., Miles, T.R., 1998. Combustion properties of
497 biomass. *Fuel Processing Technology* 54, 17–46. [https://doi.org/10.1016/S0378-3820\(97\)00059-3](https://doi.org/10.1016/S0378-3820(97)00059-3)
498
- 499 16. Jiang, X., Lu, Q., Hu, B., Liu, J., Dong, C., Yang, Y., 2018. Intermolecular interaction
500 mechanism of lignin pyrolysis: A joint theoretical and experimental study. *Fuel* 215,
501 386–394. <https://doi.org/10.1016/j.fuel.2017.11.084>
- 502 17. Kawamoto, H., 2017. Lignin pyrolysis reactions. *J Wood Sci* 63, 117–132.
503 <https://doi.org/10.1007/s10086-016-1606-z>
- 504 18. Ojha, D.K., Vijju, D., Vinu, R., 2017. Fast pyrolysis kinetics of alkali lignin: Evaluation of
505 apparent rate parameters and product time evolution. *Bioresource Technology* 241,
506 142–151. <https://doi.org/10.1016/j.biortech.2017.05.084>
- 507 19. Raveendran, K., 1996. Pyrolysis characteristics of biomass and biomass components. *Fuel*
508 75, 987–998. [https://doi.org/10.1016/0016-2361\(96\)00030-0](https://doi.org/10.1016/0016-2361(96)00030-0)
- 509 20. Richter, F., Rein, G., 2017. Pyrolysis kinetics and multi-objective inverse modelling of
510 cellulose at the microscale. *Fire Safety Journal* 91, 191–199.
511 <https://doi.org/10.1016/j.firesaf.2017.03.082>
- 512 21. Shafizadeh, F., Bradbury, A.G.W., 1979. Thermal degradation of cellulose in air and
513 nitrogen at low temperatures. *J. Appl. Polym. Sci.* 23, 1431–1442.
514 <https://doi.org/10.1002/app.1979.070230513>
- 515 22. Várhegyi, G., Antal, M.J., Jakab, E., Szabó, P., 1997. Kinetic modeling of biomass pyrolysis.
516 *Journal of Analytical and Applied Pyrolysis* 42, 73–87. [https://doi.org/10.1016/S0165-2370\(96\)00971-0](https://doi.org/10.1016/S0165-2370(96)00971-0)
517
- 518 23. Vitoussia, T., Brillard, A., Kehrl, D., Kemajou, A., Njeugna, E., Brilhac, J.-F., 2019.
519 Thermogravimetric analyses and kinetic modeling of pellets built with three
520 Cameroonian biomass. *Biomass Conv. Bioref.* <https://doi.org/10.1007/s13399-019-00558-3>
521
- 522 24. Vyazovkin, S., Burnham, A.K., Criado, J.M., Pérez-Maqueda, L.A., Popescu, C., Sbirrazzuoli,
523 N., 2011. ICTAC Kinetics Committee recommendations for performing kinetic
524 computations on thermal analysis data. *Thermochimica Acta* 520, 1–19.
525 <https://doi.org/10.1016/j.tca.2011.03.034>
- 526 25. Wang, S., Dai, G., Yang, H., Luo, Z., 2017. Lignocellulosic biomass pyrolysis mechanism: A
527 state-of-the-art review. *Progress in Energy and Combustion Science* 62, 33–86.
528 <https://doi.org/10.1016/j.pecs.2017.05.004>
- 529 26. Xu, D., Chai, M., Dong, Z., Rahman, Md.M., Yu, X., Cai, J., 2018. Kinetic compensation
530 effect in logistic distributed activation energy model for lignocellulosic biomass
531 pyrolysis. *Bioresource Technology* 265, 139–145.
532 <https://doi.org/10.1016/j.biortech.2018.05.092>
533

534

535 **Figure Captions**

536 **Fig. 1.** Experimental (solid line) and simulated through the classical (dotted line) and
537 improved (hyphened line) mass a) and mass rate b) curves for the pyrolysis of cellulose
538 under nitrogen and a temperature ramp of 5 °C/min. The Avrami-Erofeev reaction function
539 of order 2 is here used.

540 **Fig. 2.** Experimental (solid line), simulated with the classical (dotted line) or improved (large
541 hyphened line) EIPR model mass a) and mass rate b) curves for the pyrolysis of a palm nut
542 shell under nitrogen and a temperature rate of 5 °C/min.

543 **Fig. 3.** Experimental (solid line), simulated with the classical (dotted line) or improved (large
544 hyphened line) EIPR model mass a) and mass rate b) curves for the combustion of a cotton
545 sample under air and a temperature rate of 5 °C/min.

546 **Fig. 4.** Experimental (solid line), simulated with the classical (dotted line) or improved (large
547 hyphened line) EIPR model mass a) and mass rate b) curves for the combustion of a coffee
548 husk sample under air and a temperature rate of 5 °C/min.

549 **Table 1.** Process diagram of the isoconversional methods and of the Extended Independent Parallel Reaction (EIPR) Method.

	Isoconversional Methods	EIPR model
Kinetic equation	<p>A unique equation (2) which describes the evolution with respect to time of the extent of conversion α.</p> <p>The case of independent and parallel reactions is evoked in (Vyazovkin et al., 2011) for the thermal degradation of biomass and fossil fuels, which leads to a linear combination of equations (2).</p>	<p>A single first-order differential equation describes the evolution with respect to time of the mass of volatiles being emitted from each constituent and/or of the fraction of the char from each constituent which is burnt.</p> <p>The number of equations depends on the thermal degradation process (pyrolysis or combustion) and on the number of stages as observed in the experimental mass and mass rate curves. The fractions of these constituents in the raw material are also estimated from these observations.</p>
Parameters to be determined	<p>A unique set of pre-exponential factor and activation energy. These kinetic parameters are indeed global for the material, but they depend on the extent of conversion α, whence on time.</p>	<p>A single set of kinetic parameters is associated with each constituent. As many pairs of pre-exponential factors and activation energies have to be determined as the number of constituents to be considered in the EIPR model. These sets of kinetic parameters are global in time.</p>

Differential isoconversional method:

Consider (at least) three temperature ramps.

Apply the logarithm to equation (2) for each temperature ramp and change the variable:

$$\ln\left(T'_i(t) \left(\frac{d\alpha}{dT}\right)_{\alpha,i}\right) = \ln(A_\alpha f(\alpha)) - \frac{Ea_\alpha}{RT_{\alpha,i}}$$

Plot the left-hand side member in terms of $1/T$.

Apply a linear regression method.

Integral isoconversional methods:

Integrate equation (12) and change the variable:

$$g(\alpha) = \int_0^\alpha \frac{d\alpha}{f(\alpha)} = A \int_0^t \exp\left(-\frac{Ea}{RT}\right) dt \\ = \frac{A}{T'(t)} \int_0^T \exp\left(-\frac{Ea}{RT}\right) dT.$$

Introduce approximations of the right-hand side member, leading to Flynn-Ozawa-Wall, Kissinger-Akahira-Sunose... methods, (Vyazovkin et al., 2011).

Consider (at least) three temperature ramps.

Apply a logarithm.

Plot the left-hand side member in terms of $1/T$.

Apply a linear regression method.

Solve the equation or system of equations of the model with a dedicated software and minimize a chosen objective function which gathers the experimental and simulated masses and mass rates, to determine the optimal values of the pair(s) of kinetic parameters.

Process

550

551

552 **Table 2.** Initial and optimal values of the pre-exponential factor A and of the activation
 553 energy Ea determined through the classical and improved EIPR models with an Avrami-
 554 Erofeev reaction of order 2, for the cellulose pyrolysis. Error measurements and
 555 computational time.

	Classical		Improved	
	Initial value	Optimal value	Initial value	Optimal value
A (1/s)	9.00×10^{13}	9.00×10^{13}		9.96×10^{13}
Ea (kJ/mol)	190000.0	192318.6	190000.0	192968.3
l_{∞} (%/s)		0.0226		0.0200
l_2 (%/s)		0.5106		0.4761
R_m^2 (-)		0.998		0.999
R_{mr}^2 (-)		0.985		0.988
R_o^2 (-)		0.983		0.988
Computational time (s)		37.7		28.6

556

557

558 **Table 3.** Optimal values of the pre-exponential factors and of the activation energies
 559 determined through the classical and improved EIPR models, for the pyrolysis of palm nut
 560 shells. Error measurements and computational time (s).

	Classical		Improved	
	Initial value	Optimal value	Initial value	Optimal value
A_1 (1/s)	9.60×10^8	9.60×10^8		1.10×10^9
Ea_1 (kJ/mol)	119000.0	119000.0	119000.0	119000.0
A_2 (1/s)	5.0×10^7	5.0×10^7		3.3×10^7
Ea_2 (kJ/mol)	118000.0	118000.0	120000.0	118000.0
A_3 (1/s)	7300.0	7300.0		8869.0
Ea_3 (kJ/mol)	75000.0	75000.0	75000.0	75000.0
A_4 (1/s)	0.20	0.10		0.22
Ea_4 (kJ/mol)	30000.0	30000.0	30000.0	30000.0
l_∞ (%/s)		0.0240		0.0204
l_2 (%/s)		0.5235		0.3638
R_m^2 (-)		0.994		0.983
R_{mr}^2 (-)		0.905		0.954
R_o^2 (-)		0.899		0.937
Computational time (s)		2117.8		442.3

561

562

563 **Table 4.** Initial and optimal values of the pre-exponential factor A and of the activation
 564 energy Ea determined through the classical and improved EIPR models, for the combustion
 565 of a cotton sample. Error measurements and computational time.

	Classical		Improved	
	Initial value	Optimal value	Initial value	Optimal value
A_{vol} (1/s)	20000.0	19906.9		6682.0
Ea_{vol} (kJ/mol)	79000.0	79455.6	79000.0	74361.8
A_{comb} (1/(s.Pa))	7.40×10^8	7.40×10^8		6.63×10^{18}
Ea_{comb} (kJ/mol)	212000.0	212000.0	212000.0	345343.1
l_{∞} (%/s)		0.0698		0.0745
l_2 (%/s)		0.3051		0.3180
R_m^2 (-)		0.998		0.998
R_{mr}^2 (-)		0.931		0.926
R_o^2 (-)		0.929		0.924
Computational time (s)		70.2		32.6

566

567

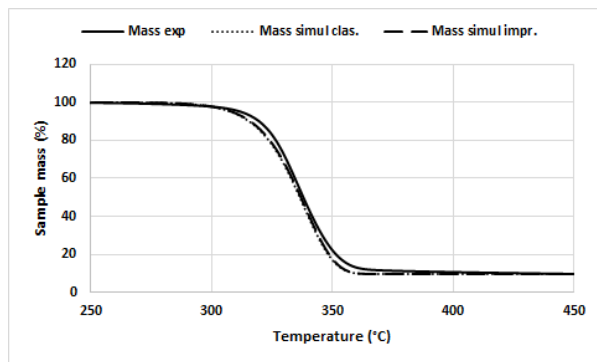
568 **Table 5.** Initial and optimal values of the pre-exponential factor A and of the activation
569 energy Ea determined through the classical and improved EIPR models, for the combustion
570 of coffee husks. Error measurements and computational time.

	Classical		Improved	
	Initial value	Optimal value	Initial value	Optimal value
$A_{vol,1}$ (1/s)	6.60×10^8	7.17×10^8		5.69×10^8
$Ea_{vol,1}$ (kJ/mol)	107000.0	107000.0	107000.0	107000.0
$A_{vol,2}$ (1/s)	6.50×10^7	7.18×10^7		8.35×10^7
$Ea_{vol,2}$ (kJ/mol)	112800.0	112800.0	112800.0	112800.0
$A_{vol,3}$ (1/s)	6.50×10^7	6.50×10^7		1.29×10^8
$Ea_{vol,3}$ (kJ/mol)	121000.0	121000.0	121000.0	121000.0
$A_{vol,4}$ (1/s)	100000.0	100043.7		116640.2
$Ea_{vol,4}$ (kJ/mol)	89000.0	89000.0	89000.0	89000.0
$A_{vol,5}$ (1/s)	1000.0	1000.4		1722.5
$Ea_{vol,5}$ (kJ/mol)	75000.0	75000.0	75000.0	75000.0
A_{comb} (1/(s.Pa))	150000.0	157826.5		149843.7
Ea_{comb} (kJ/mol)	165000.0	165000.0	165000.0	165000.0
l_{∞} (%/s)		0.0107		0.0108
l_2 (%/s)		0.2874		0.2313
R_m^2 (-)		0.998		1.000
R_{mr}^2 (-)		0.974		0.983
R_o^2 (-)		0.971		0.982
Computational time (s)		5605.5		740.5

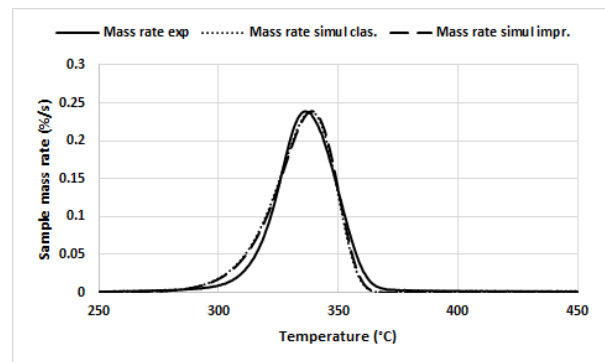
571

572

573



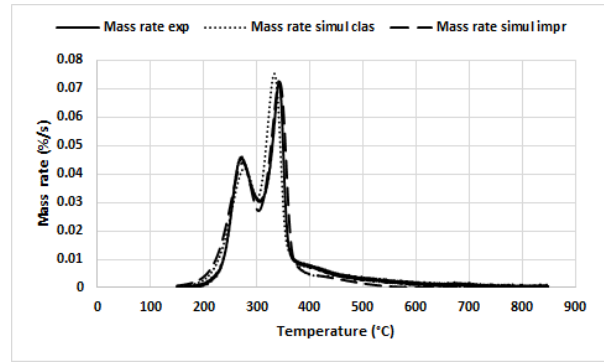
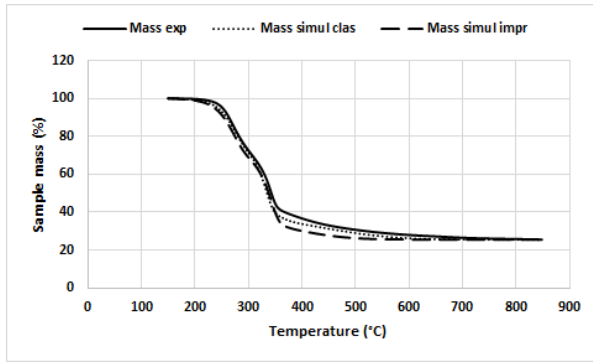
a)



b)

574 **Fig. 1.**

575

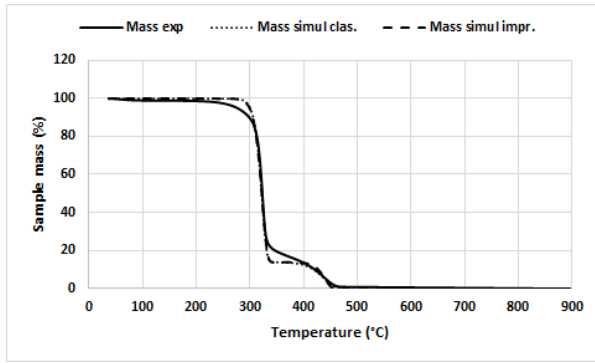


a)

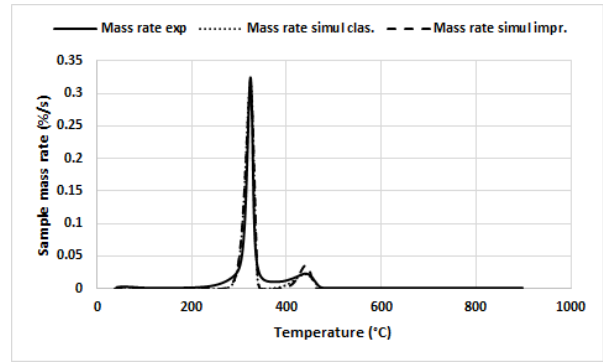
b)

576 **Fig. 2.**

577



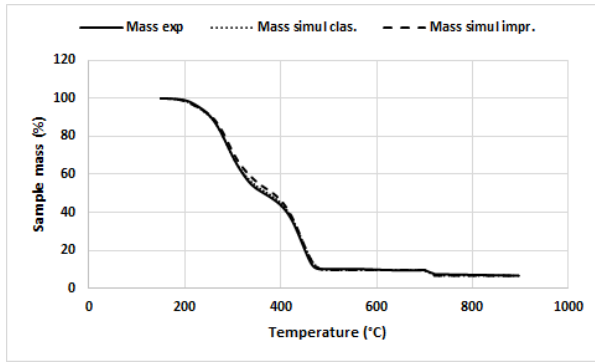
a)



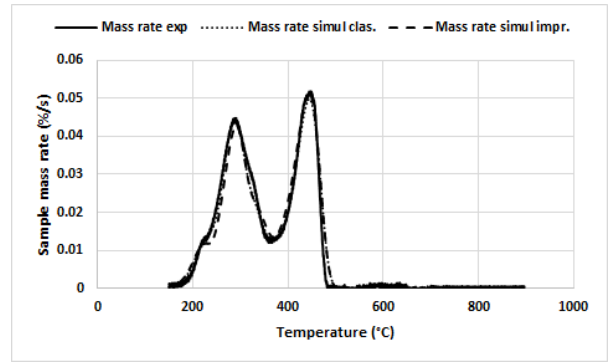
b)

578 **Fig. 3.**

579



a)



b)

580 Fig. 4.